Journal of Applied Geophysics 247 (2026) 106081

Contents lists available at ScienceDirect

Journal of Applied Geophysics

journal homepage: www.elsevier.com/locate/jappgeo

Imaging one of the largest Alpine slope instabilities with 3D seismic first-arrival traveltime tomography

Tjeerd Kiers [a,*], Cédric Schmelzbach [a,*], Hansruedi Maurer [a], Florian Amann [b], Johan Robertsson [a]

[a] Institute of Geophysics, ETH Zurich, Sonneggstrasse 5, Zurich, 8092, Switzerland
[b] Engineering Geology and Hydrogeology, RWTH Aachen, Lochnerstrasse 4-20, Aachen, 52056, Germany

ARTICLE INFO

Keywords:
Slope instability
3D characterization
Nodal array
First-arrival traveltime tomography

ABSTRACT

Understanding the internal structure and geometry of large-scale gravitational slope instabilities is crucial for hazard assessment and risk mitigation in mountainous regions. This study presents a high-resolution 2D and 3D seismic first-arrival traveltime tomography analysis of the Cuolm da Vi (CdV) slope instability, one of the largest active mass movements in the Alps. To achieve this, we conducted an extensive seismic survey, deploying over 1000 autonomous nodes across a 0.7 km^2 area and acquiring data from 144 controlled-source shots.

Our resulting 2D and 3D tomographic models reveal significant subsurface heterogeneities, including extensive low-velocity zones up to depths of 200 metres, indicative of severe rock mass disintegration. Additionally, strong lateral velocity variations persist throughout the unstable zone, further corroborating its structural complexity. Our findings align with previous studies that suggest toppling as the dominant deformation mechanism. The comparison between 2D and 3D velocity models highlights the critical role of out-of-plane effects, such as observed lateral ray bending, emphasizing the importance of 3D imaging for accurate characterization of complex instability structures.

The 2D and 3D velocity models provide important constraints for estimating the total unstable rock volume and serve as a foundation for future geotechnical analyses and hazard assessments. This study also demonstrates the feasibility and effectiveness of large-scale nodal seismic deployments in alpine terrains, paving the way for further applications in monitoring and characterizing deep-seated slope instabilities.

1. Introduction

Gravitational mass movements such as slope instabilities and landslides rank among the most destructive natural hazards worldwide. From 2004 to 2016, gravity-driven events claimed nearly 56,000 lives in 4862 events (Froude and Petley, 2018). In addition, the direct and indirect financial damages are significant and estimated to reach up to several billions of US dollars each year (Alimohammadlou et al., 2013; Sim et al., 2022). Climate change is expected to lead to a global increase of the frequency and magnitude of slope failures, due to more extreme precipitation events and processes possibly related to climate warming (Handwerger et al., 2022; Patton et al., 2019). To effectively assess risks and risk mitigation strategies arising from slope instabilities, it is critical to obtain a comprehensive understanding of the internal structure and dynamic behaviour of individual unstable slopes, as well as a thorough understanding of mass movement processes in general (Lacroix et al., 2020).

Various methods have been developed to monitor and characterize slope instabilities (Bonnard et al., 2004; Zaki et al., 2014; Intrieri et al., 2019). Surface-based approaches, such as remote sensing and geodetic tools, can offer extensive coverage and long-term monitoring, but are by definition limited to surface information (Gili et al., 2000; Rossi et al., 2016; Zhao and Lu, 2018; Shen et al., 2021). Consequently, these methods do not provide direct insights into the internal structure and dynamics of the unstable body. In contrast, geophysical methods enable non-invasive imaging and monitoring of the subsurface in 2D and 3D, providing critical insights into slope instability processes (Jongmans and Garambois, 2007; Malehmir et al., 2013; Whiteley et al., 2019). For instance, electric methods allow tracking internal moisture dynamics (Perrone et al., 2014), and ground-penetrating radar is used to investigate structural information in the shallow sub-surface (Kannaujiya et al., 2019).

Seismic methods are of particular interest for studying slope instabilities, as P- and S-wave velocities relate to subsurface elastic and

* Corresponding authors.
E-mail addresses: tjeerd.kiers@eaps.ethz.ch (T. Kiers), cedric.schmelzbach@eaps.ethz.ch (C. Schmelzbach).

https://doi.org/10.1016/j.jappgeo.2025.106081
Received 7 May 2025; Received in revised form 12 October 2025; Accepted 24 December 2025
Available online 5 February 2026

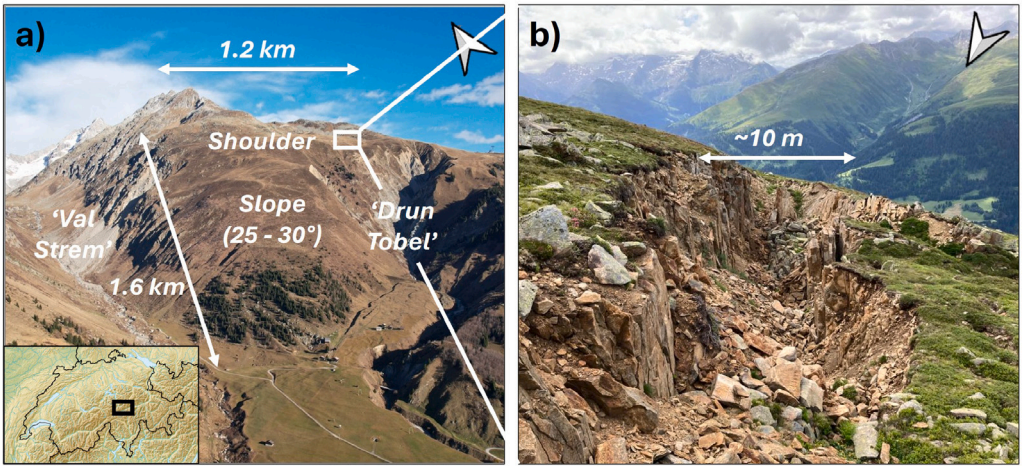

Fig. 1. Overview of the Cuolm da Vi slope instability (Sedrun, Switzerland). (a) Aerial photograph taken in summer 2022 of the Cuolm da Vi site. (b) Close-up picture (summer 2022) of the large-scale crack marking the eastern instability boundary.

mechanical properties (Aki and Richards, 2002; Uhlemann et al., 2016). Passive methods leverage natural seismicity or ambient vibrations for subsurface imaging and dynamic monitoring (Provost et al., 2018; Le Breton et al., 2021). Active seismic techniques, such as first-arrival traveltime tomography, rely on controlled sources allowing precise control over the position, magnitude, and timing of the seismic energy. Seismic first-arrival traveltime tomography has been successfully applied to characterize slope instabilities, leveraging the observation that seismic velocities are generally lower within disintegrated, unstable zones compared to the undisturbed host rock (Jongmans et al., 2000; Heincke et al., 2006; Samyn et al., 2012; Glueer et al., 2024). Nevertheless, active-source seismic experiments have predominantly been constrained to 2D investigations, with notable exceptions such as the 3D traveltime tomography studies by Heincke et al. (2006), Samyn et al. (2012) and Provenzano et al. (2025). Such 2D characterization may be insufficient as slope instabilities often exhibit significant heterogeneity, and failure processes in highly fractured and unstable crystalline rock are frequently governed by complex 3D mechanisms (Erismann and Abele, 2001; Eberhardt et al., 2001).

The 'Cuolm da Vi' (CdV) slope is one of the largest active slope instabilities in the Alps with an estimated unstable volume of 150×10^6 m^3 (Amann, 2006). The central area of the slope exhibits displacement rates of 10–20 cm/year, with pronounced annual acceleration during the April to July period, likely driven by snowmelt water. Given that toppling, rather than sliding, is suggested as the primary deformation mechanism, we refer to this feature as a 'slope instability' rather than a 'landslide' (Amann, 2006; Hungr et al., 2014).

Kleinbrod et al. (2017) conducted the only seismic study so far at Cuolm da Vi using time–frequency polarization and site-to-reference spectral ratio analysis of ambient vibrations to characterize the instability. The inversion of surface-wave dispersion curves revealed velocity profiles indicating a high level of rock mass disintegration and open fractures down to depths of at least 100 m. In addition, they observed isolated, less-fractured block-like structures in the 35–150 m depth range (Kleinbrod et al., 2017). These previous studies only comprised a small amount of sensors and did not answer critical questions on the depth extent, notably the postulated transition from disintegrated to undisturbed rock expected at 100–200 m depth (Amann, 2006).

To resolve the internal structure and spatial extent of the slope instability, we have conducted a large-scale 3D seismic refraction tomography campaign to image the CdV subsurface seismic velocity distribution and to establish a 3D model of the unstable body. We deployed more than 1000 lightweight seismic nodes covering an area of more than 0.7 km^2 including stable and unstable parts and fired 144 explosive shots within the receiver layout. Our final 2D and 3D velocity models reveal significant velocity contrasts within the CdV body likely correlating with rock integrity, that cannot be detected by surface observations. These tomograms are crucial input for estimations of the total unstable rock volume, further geotechnical analysis and corresponding risk assessment.

Table 1
Acquisition parameters of the controlled-source seismic survey in June–July 2022.

Attribute	Value
Total survey area	0.7 km^2
Sensor type	STRYDE node
Acquisition time	28 days (mid June–mid July, 2022)
GNSS time stamp interval	8 h
Sampling rate	500 Hz
Sensor bandwidth	1–125 Hz
Total number of deployed receivers	1034
Receiver spacing (hexagonal grid)	28 m
Controlled-source campaign	June 22–29, 2022
Source type	50–60 g explosives (Riodin)
Charge depth	0.4–1.0 m
Total number of sources	144
Nominal source spacing (grid & lines)	56 m

We begin by briefly reviewing the geological aspects of the Cuolm da Vi slope instability. Next, we discuss the field operations in a challenging Alpine environment to acquire a large node-number seismic data set and the measured data characteristics and quality. We present our traveltime tomography approach and resultant 2D and 3D subsurface velocity models.

2. The 'Cuolm da Vi' slope instability

The 'Cuolm da Vi' (CdV) instability is a prominent deep-seated gravitational slope deformation located in the canton Graubünden, Switzerland (Fig. 1) (Amann, 2006). CdV is positioned on a south-facing slope north of the town Sedrun in the Central Swiss Alps near the southern edge of the Aar Massif. Encompassing an area of about 1.5km^2 area and an estimated unstable volume of about 150×10^6 m^3 moving about 10–20 cm/yr in the central part, makes CdV one of the most impressive instabilities of the Alps (Amann, 2006). Generally, the CdV instability consists of a flatter shoulder part at 2200–2400 m and

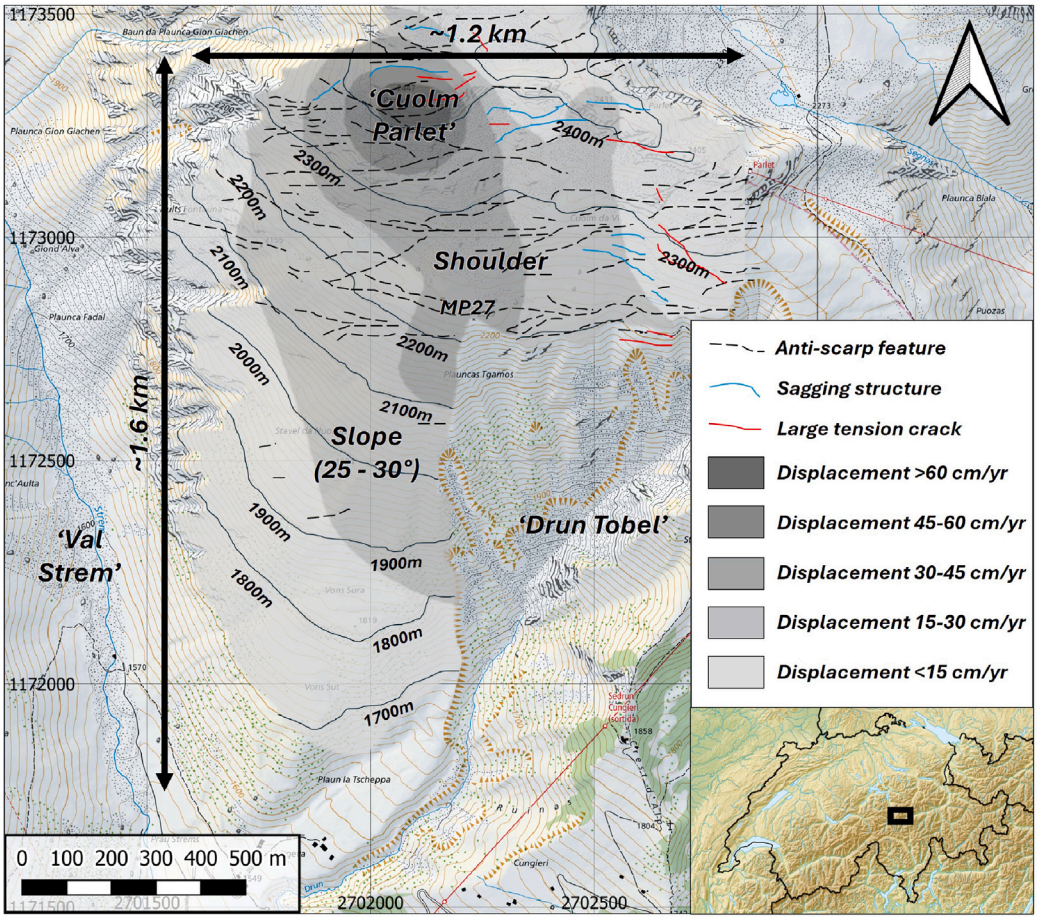

Fig. 2. Topographic map of the Cuolm da Vi instability, with superimposed annual displacement rates from 1999 to 2002 and mapped geomorphological features (adapted from Amann (2006)). Point MP27 denotes the CdV instability centre as determined by Amann (2006).

a 25–30° slope reaching the valley at approximately 1550 m (Figs. 1(a) and 2).

The highly disintegrated gneissic rocks at CdV are characterized by steeply dipping Alpine foliation and cut by multiple fracture systems (Amann, 2006). The ongoing southwest-wards propagating deformation is expressed at the surface by prominent metre to 10's of metres-scale graben structures, tension cracks (Fig. 1(b)), and sagging, indicating an overall extensional regime at the northern and eastern instability boundaries (Amann, 2006). In the central part, dominant east–west striking anti-scarp features (Fig. 2) suggest toppling in south-to-southwest wards direction. At the western and southeastern boundaries, the CdV is characterized by active gullying and frequent rock fall from shallow sources and other erosional processes in the Val Strem and Drun Tobel areas, respectively (Figs. 1(a) and 2).

Surface displacement measurements have been conducted at CdV over the past decades using ground-based global navigation satellite systems campaigns (Amann et al., 2006), correlation of images from aerial imagery (Bickel et al., 2018), and high-precision total station (tachymetry) measurements. A map with interpolated annual displacement rates during the 1999–2002 period is shown in Fig. 2. Around 2003, annual displacement rates in the centre decreased from 20-40 cm/yr by up to 50%, presumably due to exceptionally dry conditions that year (Amann, 2006). Since then, annual displacements have remained relatively stable, with the centre of the deep-seated instability around MP27 currently moving 10–20 cm annually. Note that the larger observed displacements at 'Cuolm Parlet' are predominantly due to local and shallow instability processes that do not contribute to the overall CdV dynamics (Amann et al., 2006). The displacement rates measured at CdV are characterized by a strong seasonal pattern reaching a peak towards the end of spring, likely governed by the influx of significant snow melt water (Amann et al., 2006).

3. Survey design and seismic data acquisition

3.1. Survey design

The CdV survey involved 1034 seismic point receivers (nodes) and 144 explosive sources placed around the instability's centre as illustrated in Fig. 3 and detailed in Table 1. The receiver layout was designed to cover the accessible parts of both the stable and unstable areas of the CdV rock mass, which were determined from the available geologic and geodetic data (Amann et al., 2006). The survey did not include the largely inaccessible fast-moving Cuolm Parlet area (Fig. 3) where the displacement is dominated by local, shallow instabilities independent of the CdV deep-seated deformations (Amann, 2006).

We arranged 878 receiver points in an L-shaped hexagonal grid with a nominal 28 m receiver spacing (Fig. 3). A hexagonal grid was chosen because this grid results in equal point spacing along lines in three directions. Furthermore, because of the shape of CdV, the hexagonal layout resulted in several long continuous southwest–northeast receiver lines crossing the entire slope, while at the same time providing a regular and dense coverage of the shoulder section with east–west running lines. This receiver grid covered an area of about 0.7 km^2 with maximum extensions of 1.0 km and 1.5 km in east–west and southwest–northeast direction, respectively. Additionally, six receivers were used

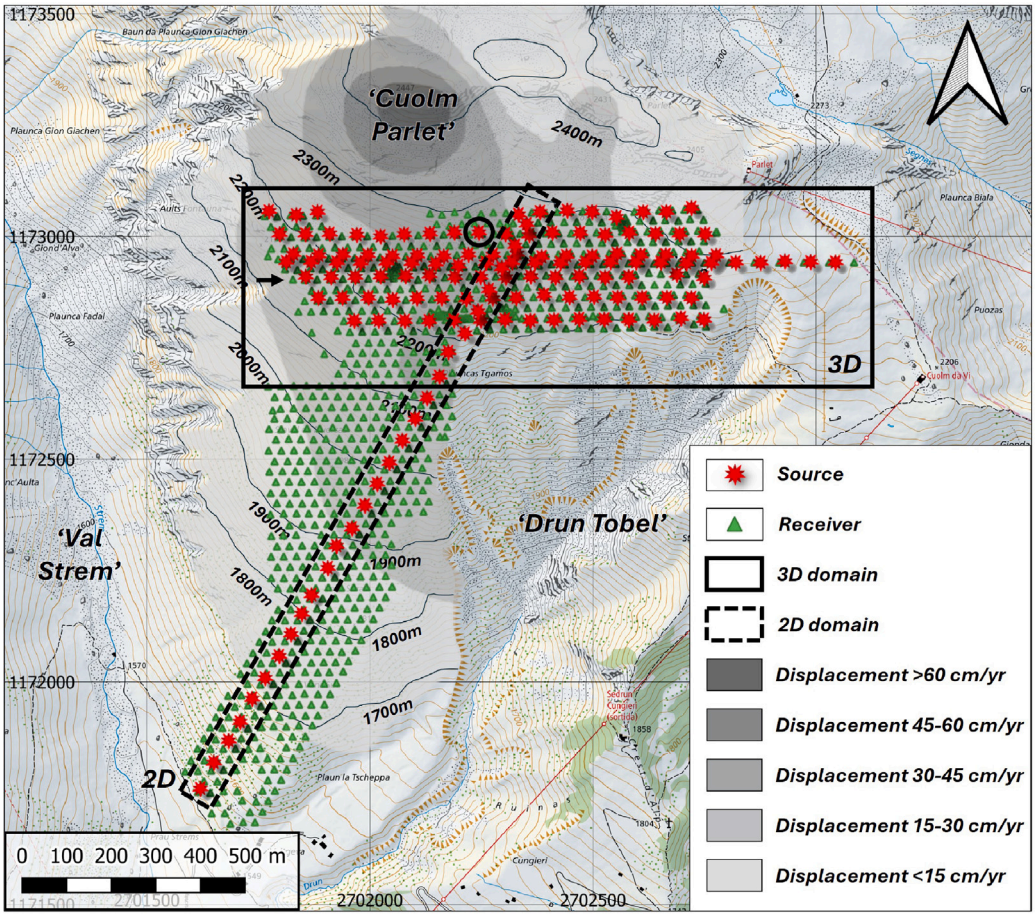

Fig. 3. Topographic map of Cuolm da Vi overlaid with the average annual displacement rate from 1999–2002 (adapted from Amann (2006)). Red stars mark the source grid on the CdV shoulder as well as two additional source lines. Green triangles indicate the receiver grid layout from June–July 2022. The 2D and 3D inversion domain are outlined with a dashed and solid box, respectively. The black circle and arrow denote the source and west–east receiver line used in Fig. 4. (For interpretation of the references to colour in this figure legend, the reader is referred to the web version of this article.)

for the extension to the east, 50 for several small-scale arrays, and 100 for the comparison between the nodes and the Distributed Acoustic Sensing acquisition (Kiers et al., 2026).

3.2. Continuous seismic data acquisition

All 1034 deployed autonomous seismic nodes manufactured by STRYDE are characterized by their small dimensions and weight of 150 g (Manning et al., 2018; O'toole et al., 2024). These sensor characteristics allowed a highly efficient deployment in the challenging alpine terrain at CdV, which was completed within 4 to 5 days. Each STRYDE node was used to record the ground acceleration in the vertical direction using a sampling rate of 500 Hz. The entire data acquisition period lasted for approximately 28 days from mid-June to mid-July 2022. An overview of the survey acquisition parameters is provided in Table 1.

We programmed each node to record a GNSS time stamp every eight hours to correct for the internal clock drift due to, for example, temperature variations. We chose this GNSS sampling interval as an adequate trade-off: it limited the maximum timing inaccuracy to 1 ms in an extreme case, while minimizing additional sensor operations to conserve battery power, thereby maximizing the acquisition time window to 28 days. Generally wet soil conditions in combination with a high grass cover negatively affected the GNSS-reception of a large number of nodes. To improve the GNSS-reception, we planted the nodes with approximately a quarter of the node body above the surface to ensure proper GNSS-response. This deployment style increased the susceptibility of the nodes to environmental noise such as wind and temperature variations. The recordings of a small number of nodes (<5%) were affected by GNSS-timing issues despite all efforts outlined above and were excluded from the further processing.

3.3. Acquisition of the controlled-source data set

A controlled-source campaign was conducted between 22nd and 29th of June 2022 (Table 1). Explosive charges of 50–60 g of Riodin were fired in 0.4–1 m deep shot holes, of which we obtained the exact source timing (t_0) by placing three dedicated nodes 1 m around the source shot hole and picking the t_0-time. The significant variation in shot hole depth was due to strongly varying subsurface conditions. Explosive charges of 50–60 g proved to be sufficient to enable large-offset (>500 m) traveltime observations without generating excessive shot hole blow-out. The majority of the sources constituted a hexagonal grid on the CdV shoulder with a nominal 56 m spacing, corresponding to twice the nominal receiver distance. Due to the steep and challenging terrain in the CdV slope region (Figs. 1(a) and 2), it was practically unfeasible to extend the source grid to this area. Instead, we acquired two additional source lines: one east–west line crossing the CdV shoulder and one southwest–northeast line spanning the entire CdV slope (Fig. 3).

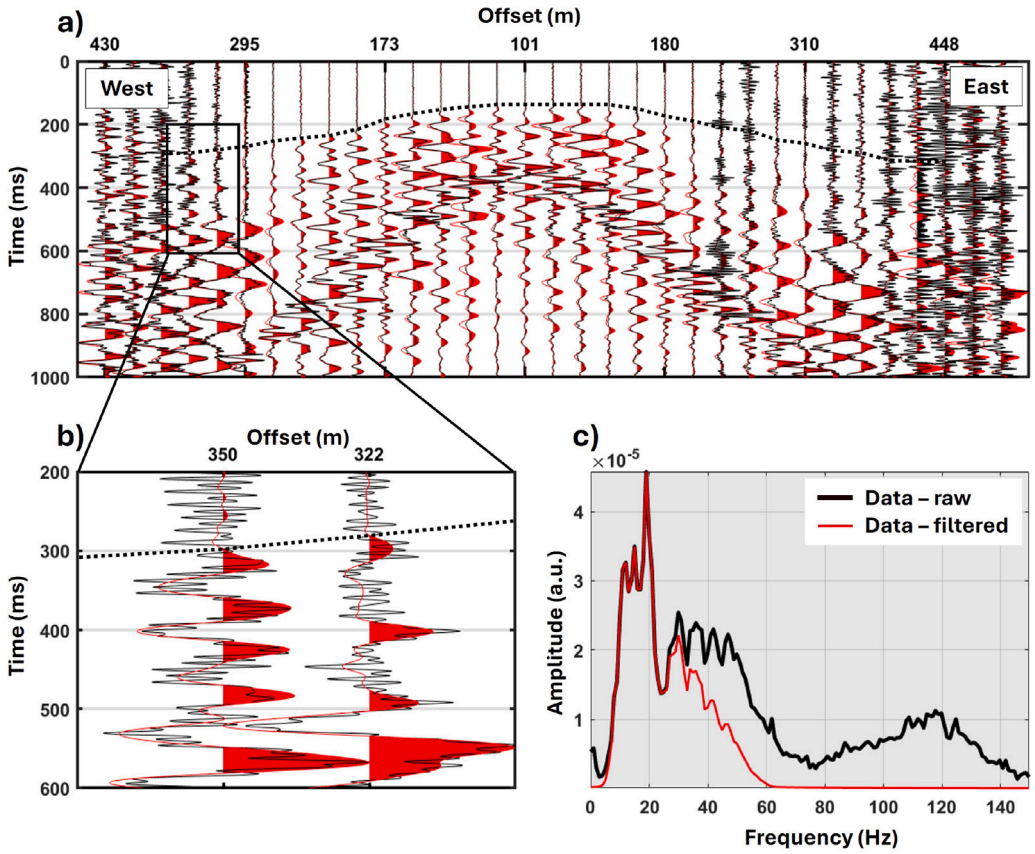

Fig. 4. Comparison of the raw (black) and bandpass filtered data (red) for source location 10209 (black circle in Fig. 3). (a) Source gather recorded by the west–east receiver line 207 (black arrow in Fig. 3). The raw data traces are shown in black and bandpass filtered traces are superimposed in red (Ormsby-filter 7.5–25 Hz). The first-arrival traveltime picks are marked by a dashed black line. (b) Display of a zoomed window for two mid-offset traces showing the comparison of raw and filtered data in more detail. (c) Amplitude spectra of the raw and bandpass filtered data. (For interpretation of the references to colour in this figure legend, the reader is referred to the web version of this article.)

4. Seismic and traveltime data

4.1. Seismic data quality and signal characteristics

Common-source and common-receiver gathers were screened for low-quality waveform recordings. The data from eight malfunctioning receivers and three low-quality sources were excluded from further processing. Fig. 4 presents a representative source gather with corresponding amplitude spectra for source position 10209, recorded by the west–east receiver line 207 (denoted by a black circle and arrow in Fig. 3, respectively).

The signal-to-noise ratio (SNR) of the raw data is generally adequate to identify the first-arrival onsets up to offsets of 200–300 m. For larger offsets, however, the first arrival with signal frequencies between around 10 and 20 Hz is often obscured by incoherent high- and low-frequency noise (Figs. 4(a) and (b)). The high-frequency noise (>40 Hz) is presumably related to wind affecting the nodes, while significant low-frequency instrument noise (<5 Hz) was observed during some periods of the day. The prominent appearance of these environmental noises (e.g., temperature variations) is likely related to the fact that a significant part of each node was exposed above the surface.

4.2. Traveltime picking and uncertainties

The traveltimes for the 2D and 3D analysis were manually picked using the ProMAX/SeisSpace software (Landmark-Halliburton). To pick the first-arrival traveltimes, we applied a Ormsby bandpass filter with wide ramps (3-7.5–25-62.5 Hz) in order to improve the SNR of the first-arrivals (Fig. 4). The effects of bandpass filtering were thoroughly examined by comparing filtered and unfiltered seismic data, to ensure consistency in traveltime picking (Fig. 4(b)).

The first-arrival traveltime data for the 2D inversion were extracted from source gathers consisting of three parallel receiver lines (Fig. 3). To establish the data set for the 3D analysis, we exploited the hexagonal receiver grid structure and picked the traveltimes first on east–west running receiver lines before revising the picks in northwest–southeast and southwest–northeast running receiver lines for consistency (Fig. 3).

We could determine a total of 2188 and 33,423 first-arrival traveltimes for the 2D and 3D inversion, respectively, of which the distribution with respect to source–receiver offset is shown in Fig. 5. For both the 2D and 3D data set, more than 80% of the possible traveltimes could be picked for source–receiver offsets <300 m. Beyond 300 m offset, the fraction of picked traveltimes reduces significantly to approximately 10% for 700–800 m offset. Slight differences between the 2D and 3D data set are presumably related to variations in subsurface conditions between the shoulder and slope area.

We initially designed the source grid so that each source location would be positioned at the centre of the equilateral triangles formed by the hexagonal receiver grid, ensuring equal distances to the three nearest receivers. However, inaccuracies arose from converting receiver coordinates from the Swiss LV95 to the global WGS84 coordinate system, which was necessary for compatibility with the STRYDE deployment system. This conversion introduced a systematic stretching of the implemented receiver grid in the southwest–northeast direction. This gradually increasing shift reached up to 10 m in the northeastern part of the survey area, resulting in approximate co-location of certain source and receiver positions. To ensure accurate geometry information for processing, all receiver positions were precisely surveyed in

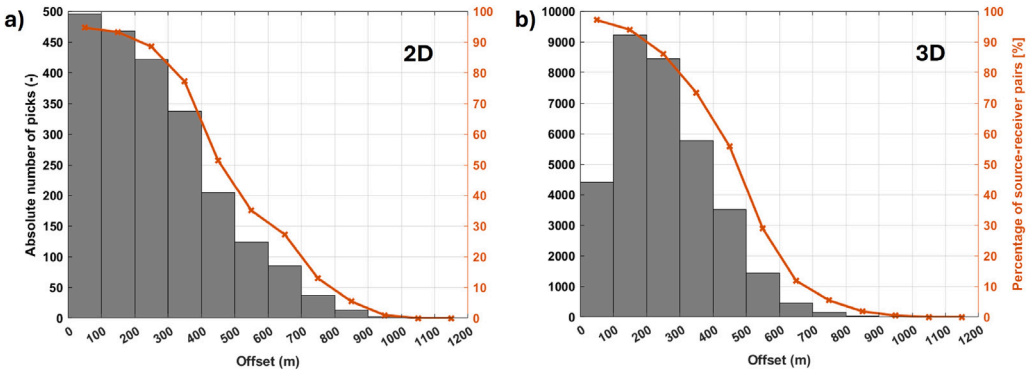

Fig. 5. Traveltime distribution with respect to source–receiver offset for both the (a) 2D and (b) 3D domain. The grey histogram plot shows the absolute number of traveltime picks in the respective offset bin. The red line marks the percentage of source–receiver pairs for which a traveltime could be picked. For the 3D case, note the lower absolute number of picks in the 0–100 m bin, which is due to the array geometry and associated limited amount of available source–receiver pairs. (For interpretation of the references to colour in this figure legend, the reader is referred to the web version of this article.)

the LV95 coordinate system prior to node retrieval. The unintended partial source–receiver overlap allowed us to exploit source–receiver reciprocity (Schmelzbach et al., 2008) to assess data uncertainty by analysing traveltime differences for interchangeable source–receiver pairs. A half-normal distribution fitted to the absolute traveltime differences yielded standard deviations of 10.8 ms (from 96 pairs) and 9.2 ms (from 1896 pairs) for the 2D and 3D data sets, respectively. These uncertainty estimates of approximately 10 ms correspond to roughly one-fifth of the dominant signal period (Fig. 4(c)).

5. First arrival travel time tomography

5.1. 2D and 3D inversion domain

For the subsequent 2D and 3D inversion, we defined a 2D and 3D domain with corresponding subset selections of sources and receivers (Figs. 3 and 6). The 2D domain runs from the presumably stable valley bottom in the southwest along the entire CdV slope towards the northeast spanning 1550 m, where it crosses the most active part of the CdV shoulder (Fig. 3). This 2D configuration consists of the southwest–northeast source line and three adjacent parallel receiver lines including a total of 27 sources and 158 receivers (Fig. 6(a) and Table 2).

The 3D domain encompasses both the presumed stable and unstable regions of the CdV shoulder (Fig. 3) and includes all available sources and receivers within this area (Fig. 6). This domain covers an area of 1370 x 430 m and comprises the northern section of the hexagonal receiver grid, along with the additional small-scale receiver deployments at the CdV shoulder, totalling 490 receivers. The CdV shoulder source grid, supplemented by two additional source lines, provided 125 available sources, all of which were utilized for the 3D inversion (Fig. 6 and Table 2).

5.2. Inversion strategy

Our first-arrival traveltime tomography algorithm is based on minimizing the misfit between observed and predicted data (Lanz et al., 1998). We defined an initial velocity model, employed a forward solver for traveltime computation and ray tracing, applied suitable regularization and solved the subsequent inverse problem iteratively. This approach generally applies to both the 2D and 3D inversion case (Table 2). Note that for the 2D domain, the sources and receivers are not located exactly along a single straight line (Fig. 6(a)). Therefore, we projected the source and receiver locations onto a line and corrected the observed traveltimes for imposed path length changes using geometry relations.

Table 2
2D and 3D inversion parameters.

Parameter	2D	3D
Domain dimensions	1550 x 1000 m	1370 x 430 x 700 m
No. of included sources	27	125
No. of included receivers	158	490
No. of first-arrival picks	2188	33,432
Forward grid dimensions	1 x 1 m	4 x 4 x 4 m
Starting model surface velocity (V_0)	400 m/s	400 m/s
Starting model constant k	22 (m/s)/m	22 (m/s)/m
Starting model constant n	1.05	1.05
Air velocity	330 m/s	330 m/s
Inverse cell dimensions (at surface)	8 x 4 m	8 x 8 x 4 m
Inverse cell size increase factor	1.05	1.05
No. of inverse cells	3474	119,728

5.3. Initial model

We established a starting model for both the 2D and 3D inversion domain (Fig. 6 and Table 2), based on the same 1D so-called Evjen velocity function as described in Greenhalgh and King (1981):

$$V(z) = V_0(1 + kz)^{1/n}, \quad (1)$$

where $V(z)$ is the P-wave velocity at depth z below the surface, V_0 marks the velocity at the surface ($z = 0$) and k and n are two constants defining the velocity increase with depth. From very-short offset (<10 m) travel time observations, we obtained a surface velocity V_0 of 400 m/s. The other parameters were determined by trial-and-error comparison of modelled and observed traveltime data, resulting in $k = 22$ and $n = 1.05$ (Table 2). The surface topography defining $z = 0$ was implemented by assigning a fixed air velocity of 330 m/s to all model cells above the surface.

5.4. Solution to the forward problem

To solve the 2D and 3D forward problem, we followed Podvin and Lecomte (1991), including the revisions suggested by Tryggvason and Bergman (2006), and employed the backtracing algorithm outlined by Li et al. (2018) for ray computation. We defined square and cubic grids with side lengths of 1 m and 4 m for the 2D and 3D forward-modelling grid, respectively (Table 2). These grid sizes enabled stable traveltime computations while staying within computational memory limits for the both 2D and 3D case.

5.5. Solution to the inverse problem

We solved the non-linear and underdetermined inverse problem following Lanz et al. (1998) by iteratively finding the solution to the

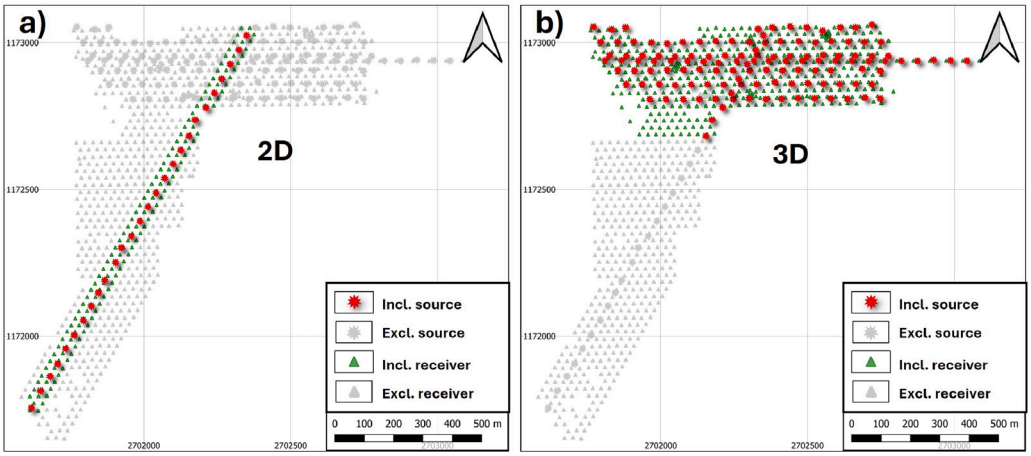

Fig. 6. Overview of the sources and receivers that are included in the 2D and 3D inversion workflow. (a) The 2D configuration consists of 27 sources and three parallel adjacent receiver lines containing 158 receivers. (b) The 3D layout includes 125 sources and 490 receivers that constitute a source and receiver grid at the CdV shoulder.

following system of equations using a Gauss–Newton scheme:

$$\begin{pmatrix}\mathbf{t}\\ \mathbf{h}\end{pmatrix} = \begin{pmatrix}\mathbf{L}\\ \mathbf{D}\end{pmatrix}\mathbf{s}, \tag{2}$$

where **L** denotes the Jacobian matrix of size $n \times m$ (number of data points × number of inverse cells), **t** the observed travel times, **D** and **h** the regularization constraints, and **s** the unknown slowness values. As described by Maurer et al. (1998), the matrix **D** consists of an upper part, which is a diagonal $m \times m$ matrix used for damping constraints, and a lower part, constituting an $m \times m$ matrix representing the first-order smoothing operator. Similarly, the vector **h** is composed of an upper part with the initial or previously estimated slownesses and a lower part containing zeros. The right-hand side matrix of Eq. (2) is typically sparse, allowing the system of equations to be effectively solved using the LSQR algorithm proposed by Paige and Saunders (1982). After each update of the velocity model, the predicted travel times and ray geometry are recomputed to update **L**.

We used rectangular and cuboid cells for the inverse problem parametrization that increase in size with depth below the surface (Table 2). For the 2D and 3D inversion problems, we selected cell dimensions at the surface of 8 x 4 m and 8 x 8 x 4 m, respectively (horizontal times vertical dimension). To account for decreasing ray coverage with depth, we increased the cell dimensions in the depth (z) direction by a factor of 1.05 for each new layer. The parameters controlling the damping and smoothness constraints (Eq. (2)) were determined by trial-and-error, to identify adequate parameter sets that allowed fitting the observed traveltimes to within the estimated uncertainties of 10.8 and 9.2 ms for the 2D and 3D case, respectively. For our preferred regularization set, smoothing dominates over damping by a factor of two for both the 2D and 3D inversions.

6. Results of the 2D inversion

6.1. 2D velocity model

Our final 2D P-wave velocity model, obtained after 15 iterations and converging to a traveltime misfit RMS of 8.18 ms, is presented in Fig. 7. In the shallowest 20 m, velocities range between 500 and 1000 m/s, with slightly higher values near the slope bottom area (southwest of the 2D profile). At depths greater than 30 m, we observe significant lateral velocity variations. In the lower part of the profile, up to approximately $x = 500$ m profile distance, seismic velocities increase notably with depth, from around 1000 m/s near the surface to over 3000 m/s at 50 m depth. In contrast, northeast of $x = 500$ m, a triangular-shaped low-velocity zone (<2000 m/s) extends across much of the profile, reaching depths of up to 200 m at the top of the profile (shoulder area).

6.2. 2D velocity model assessment

The traveltime residuals (observed minus modelled traveltimes) as a function of offset are plotted for the initial and final model in Fig. 8(a) and (b), respectively. The corresponding velocity models are presented in Fig. 8(c) and (d). The large spread of initial traveltime residuals, with an RMS of 57.6 ms, indicates significant lateral velocity variations that are not explained by the starting model. Positive residuals are likely associated with the extensive low-velocity region. Through 15 iterations, the traveltime misfit is reduced to an RMS value of 8.18 ms, which is slightly lower than the estimated traveltime uncertainty of 10.8 ms derived from the reciprocity analysis. Most rays are concentrated within the uppermost 100 m (Fig. 8(d)), as a consequence of the source–receiver offset distribution (Fig. 5(b)) and the strong velocity gradient in the shallow subsurface. At greater depths, however, ray path coverage becomes more laterally variable, with only a limited number of rays crossing the deep sections of the low-velocity region in the shoulder area, making this region less well constrained.

7. Results of the 3D inversion

Horizontal slices extracted from the final 3D P-wave velocity volume are shown in Fig. 9(a). A general trend of velocity increase with depth is evident, ranging from approximately 500–1000 m/s at the surface to 2500–4000 m/s at a depth of 200 m. Notably, substantial lateral velocity heterogeneities are present at each depth level. At a depth of 50 m, alternating elongated positive and negative velocity anomalies are particularly prominent in the northeastern part of the volume, with lateral velocity contrasts spanning 300–700 m/s. At depths around 150 m, we note even more pronounced lateral velocity variations. These variations are characterized by a low-velocity zone in the central part of the volume surrounded by markedly higher velocities, especially concentrated in the north to northwestern area adjacent to the low-velocity zone.

Vertical slices of the 3D P-wave model are presented in Fig. 10. These slices correspond to the three east–west profiles along the dashed lines in Fig. 9. The vertical slices reveal lateral velocity heterogeneities similar to those observed in the depth slices discussed above. In the central part of the CdV shoulder (middle row, around 2.7024×10^6 m easting), we observe a distinct velocity transition between depths of 150 m and 200 m, where velocities rapidly increase from less than 2000 m/s to over 3500 m/s. However, more towards the west and east, as well as along the northern and southern profile (top and bottom row, respectively), this transition is more gradual and occurs at shallower depths (100–150 m).

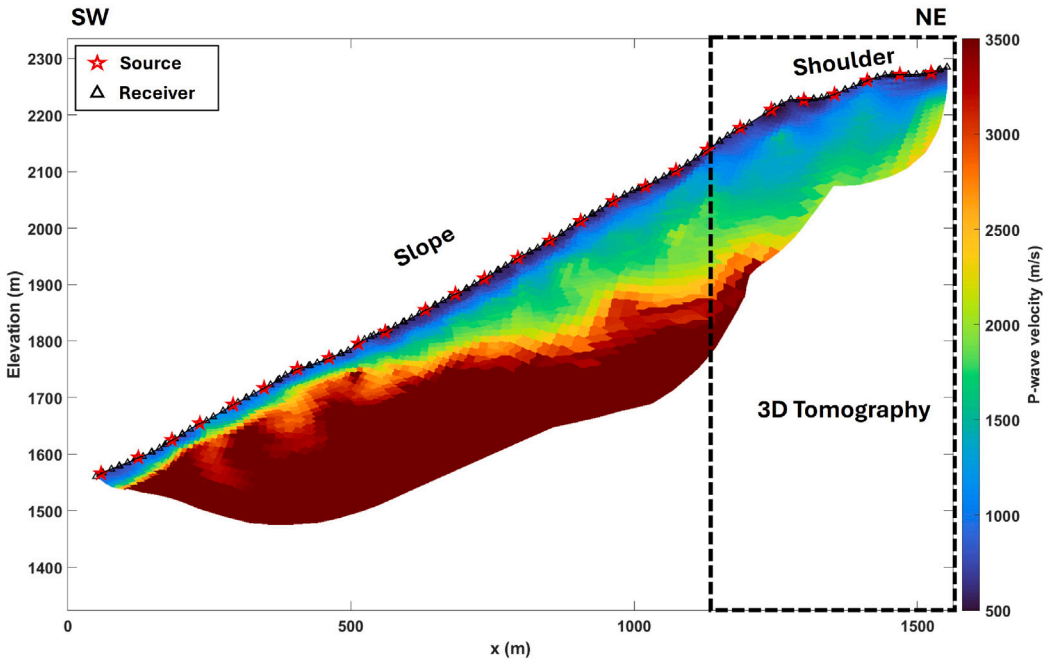

Fig. 7. Final 2D P-wave velocity model after iteration 15 (see Figs. 3 and 6(a) for geometry). Only cells covered by rays are shown. Source and receiver locations projected onto the 2D inversion plane are marked as red pentagrams and black triangles, respectively. (For interpretation of the references to colour in this figure legend, the reader is referred to the web version of this article.)

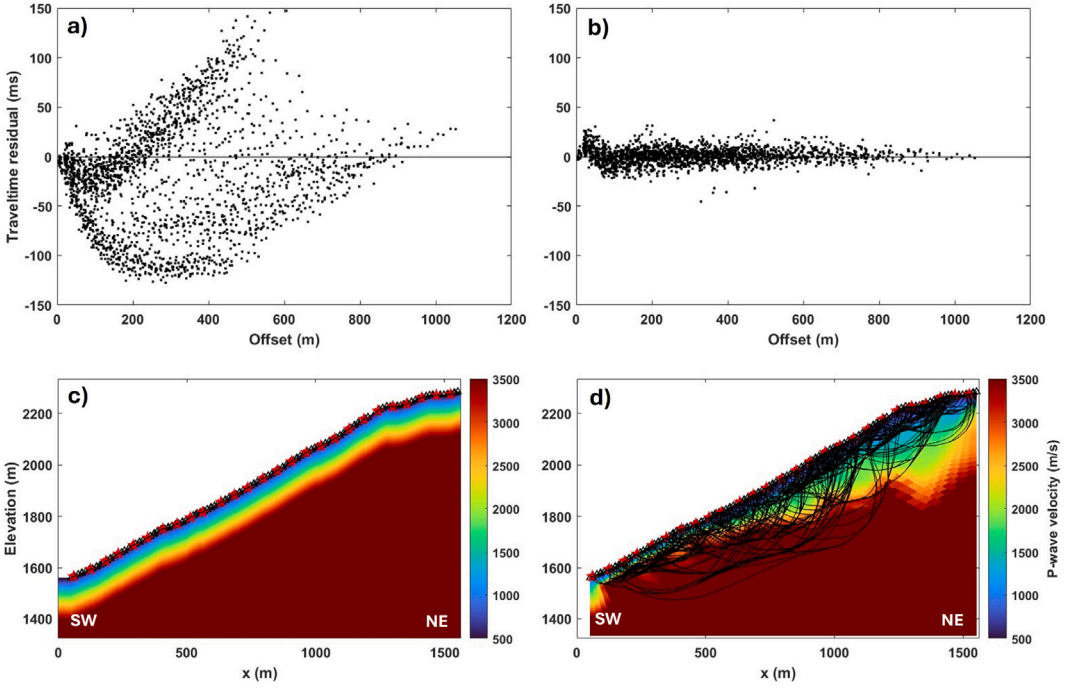

Fig. 8. Traveltime residuals (observed minus modelled traveltime) for (a) the starting model (RMS of 57.6 ms) and (b) the final model (RMS of 8.18 ms), plotted as a function of offset. (c) 2D starting model based on a 1D depth-dependent Evjen function starting at the surface (Table 2). All cells above the surface topography have a fixed air velocity value (330 m/s) and are plotted as white. Sources and receivers are marked by red pentagrams and black triangles, respectively. (d) Final 2D velocity model (same as Fig. 7), but now including non-ray-covered cells and with superimposed ray paths. (For interpretation of the references to colour in this figure legend, the reader is referred to the web version of this article.)

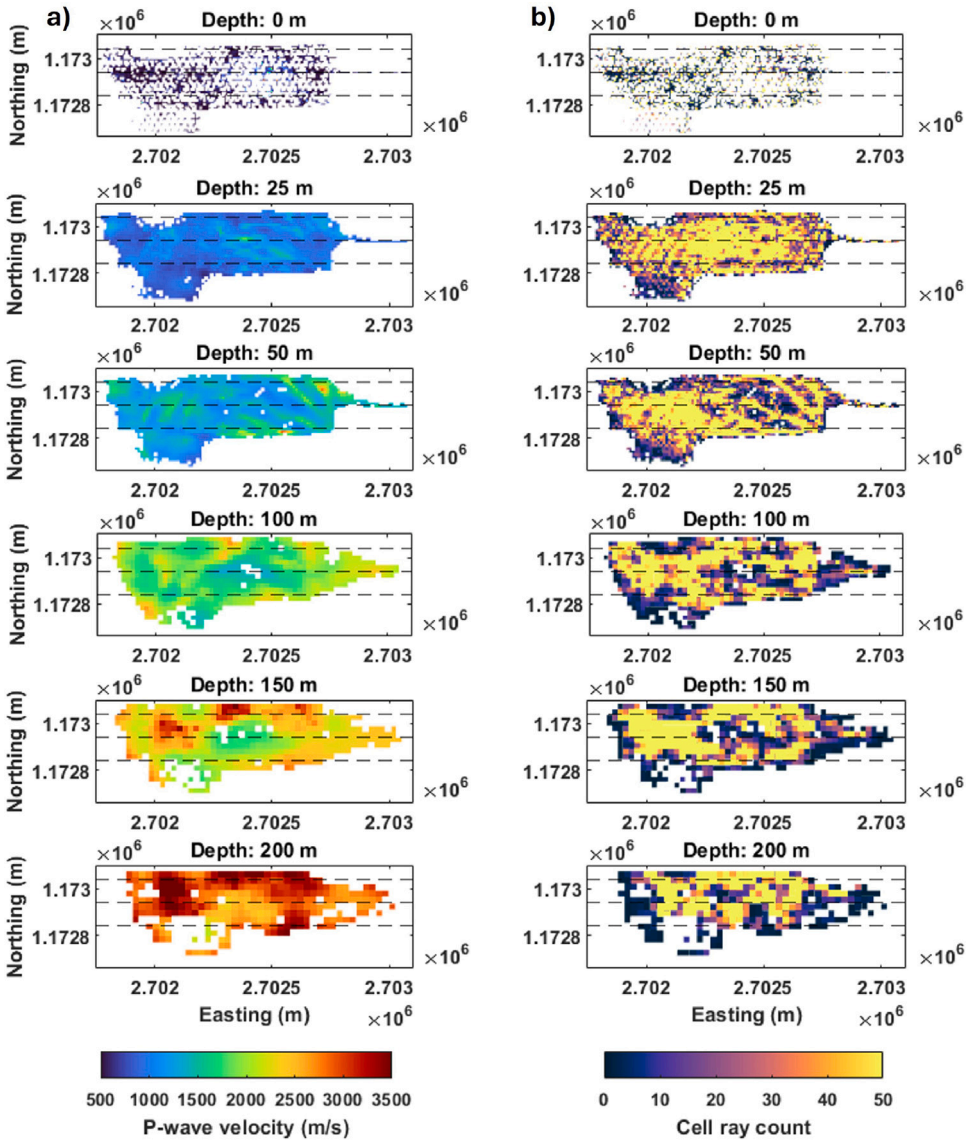

Fig. 9. Final 3D inversion results after 30 iterations (for geometry, see Figs. 3 and 6(b)). (a) Horizontal slices extracted from the 3D velocity model at a constant depth beneath the surface topography. Only ray-covered cells are shown. (b) Corresponding cell-based ray count for the slices shown in (a). The profile lines of the vertical 3D model slices in Fig. 10 are indicated by dashed lines.

We further note that in the easternmost section of the 3D domain, which is best covered by the middle profile, relatively higher velocities (2300–2700 m/s) are present at shallow depths (50–100 m). The lateral transition from these higher velocities in the east to the central low-velocity zone occurs between 2.7026×10^6 m and 2.7027×10^6 m easting (also visible in top profile). This transition coincides with the boundary between the stable and moving parts of the CdV shoulder (Fig. 2) and aligns with the location of large opening cracks at the surface (Fig. 1(a)).

7.1. Assessment of the 3D model

The traveltime residuals for both the initial and final 3D model are shown as a function of source–receiver offset in Fig. 11(a) and (b), respectively. After 30 iterations, the spread of residuals was effectively reduced, with the RMS decreasing from 23.5 to 9.76 ms. This final RMS value closely aligns with the estimated uncertainty of 9.2 ms derived from the reciprocity analysis. Furthermore, we note that the initial RMS of 23.5 ms for the 3D data set is considerably lower than the value of the 2D data set (initial RMS of 57.6 ms), despite both starting models being constructed using the same Evjen function (Eq. (1)).

As velocity anomalies and ray coverage generally correlate in ray-based travel time inversions, we evaluated the 3D ray distribution for the final model. In Figs. 9(b) and 10(b), we present the cell ray count of the final 3D model for the horizontal and west–east vertical slices, respectively. At the surface level (0 m depth), ray paths primarily intersect surface cells that contain either a source or receiver, due to their steeply dipping behaviour. By approximately 25 m depth, we observe near-complete lateral ray coverage, likely due to the influence of small-offset picks in an omnidirectional sense. Adequate ray coverage extends down to 200 m depth, suggesting that the velocity model remains predominantly data-driven within this range. However, note that the cell ray count displayed in Figs. 9(b) and 10(b) does not equate to ray density, due to the aforementioned increase in cell size with depth. As expected, high-velocity anomalies correlate with elevated ray counts, as high-velocity perturbations often accommodate the smallest source–receiver traveltime However, low-velocity regions are also intersected by rays, as evidenced by the absence of unsampled (white) cells in Figs. 9(a) and 10(a).

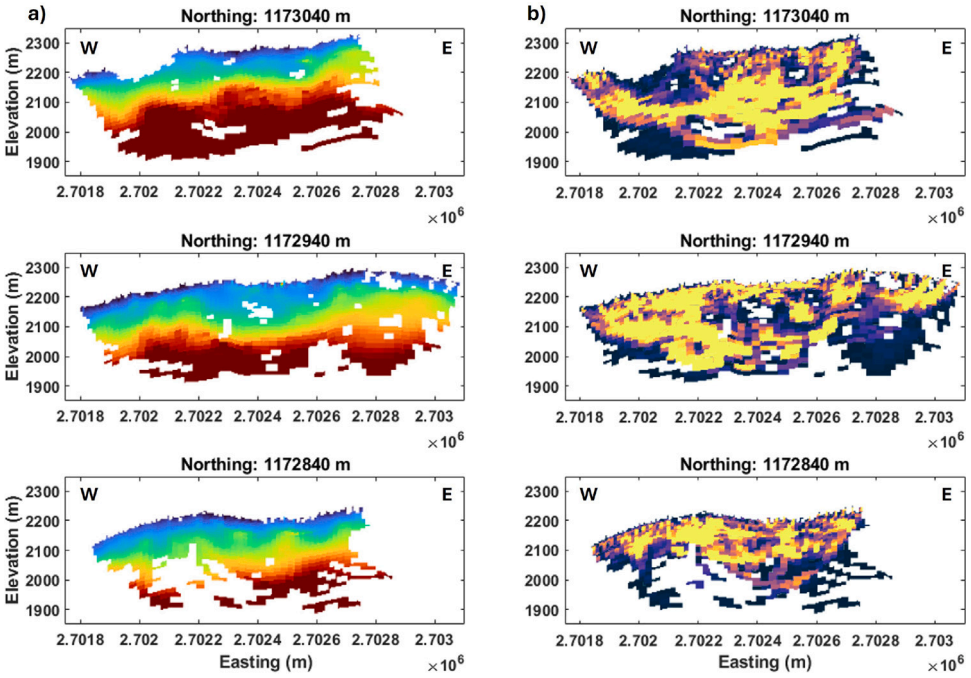

Fig. 10. Vertical slices of the final 3D model along the three profile lines indicated by dashed lines in Fig. 9. (a) West–east slices of the 3D velocity model, displaying only ray-covered cells. (b) Corresponding cell-based ray count for the slices shown in (a).

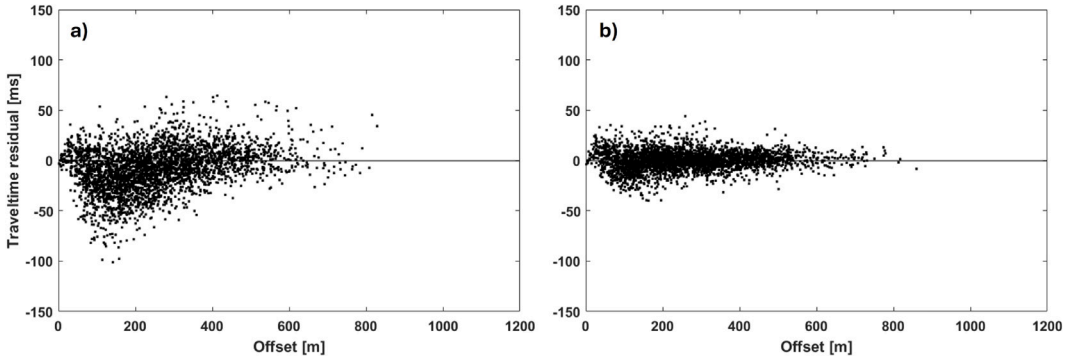

Fig. 11. Traveltime residuals (observed minus modelled traveltimes) as a function of offset for (a) the starting model (RMS: 23.5 ms) and (b) the final model (RMS: 9.76 ms). For clarity, only every 10th residual is plotted.

These observations are further supported by Fig. 12, which illustrates the source–receiver ray path geometry for shot location 30024 in the three orthogonal planes. In Figs. 12(b) and (c), the steeply dipping ray paths near the surface are evident. Note that this steep dipping and associated velocity gradient is with respect to the local topography rather than the vertical axis. Furthermore, Fig. 12 highlights the correlation between ray coverage and velocity anomalies. While ray paths converge through higher-velocity regions, the distribution remains sufficiently uniform to ensure coverage of lower-velocity zones as well. At depths exceeding 200 m, ray sampling becomes increasingly sparse, with only a small amount of large-offset, divergent ray paths intersecting these model cells (Fig. 12(b)). Therefore, these deeper model regions are only constrained by a limited number of data points and consequently, should only be considered for interpretation with caution.

8. Discussion

8.1. Comparison of the 2D and 3D subsurface models: out-of-plane effects

The coincident 2D and 3D velocity models enable us to evaluate the consistency between the independently derived 2D and 3D inversion models of a largely identical traveltime data set. Additionally, they provide an opportunity to investigate the effects of lateral heterogeneity and out-of-plane effects on the 2D models (for overlap geometry, see Figs. 3, 6, and 7). The relative velocity differences between the 2D model and a co-located plane extracted from the 3D model are presented in Fig. 13(a), where positive values indicate higher velocity values in the 2D model relative to the 3D model, and vice versa. Within the upper 100 m below the surface, such positive velocity differences in the range of 0%–30% dominate, except for two small regions of negative difference at approximately 1300 m and 1475 m profile distance. Below 100 m depth, velocity differences are generally smaller and predominantly negative, indicating slightly higher velocities in the 3D model.

The relatively higher shallow velocities in the 2D model compared to the co-located 3D model plane are predominantly due to lateral ray bending and associated out-of-plane effects, as illustrated in Fig. 13(b). We observe in Fig. 13(b) that, for sources included in the 2D inversion, rays laterally bend along high-velocity anomalies in a fully 3D sense. When projected onto a 2D plane, this results in artificially elevated velocity values along the 2D profile relative to the more accurate

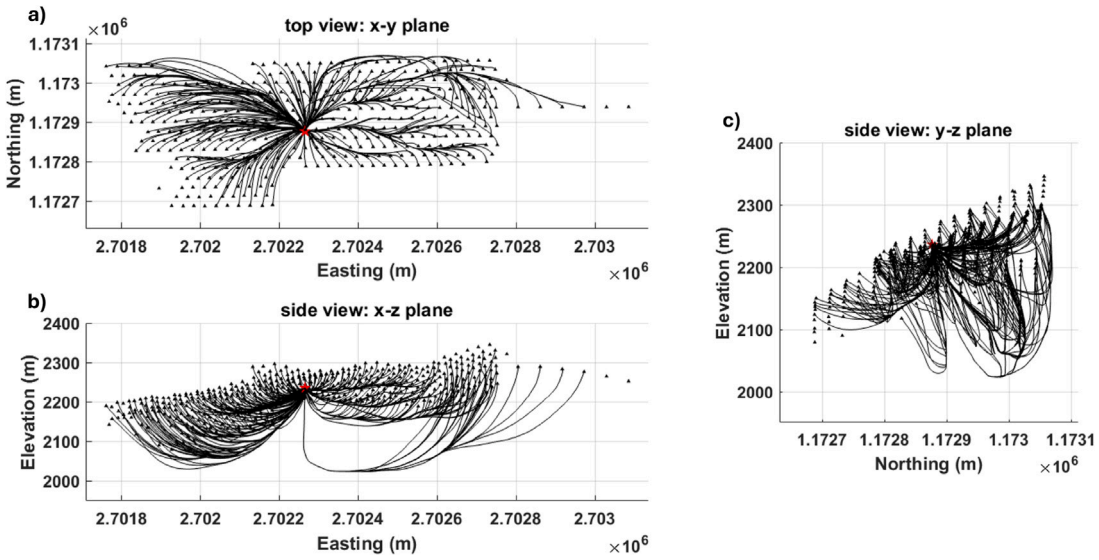

Fig. 12. Source–receiver ray paths for shot location 30024 projected onto the three orthogonal planes. The source and receiver positions are denoted by a red pentagram and black triangles, respectively. Receivers without connecting ray paths represent source–receiver pairs for which the first-arrival could not be picked. (For interpretation of the references to colour in this figure legend, the reader is referred to the web version of this article.)

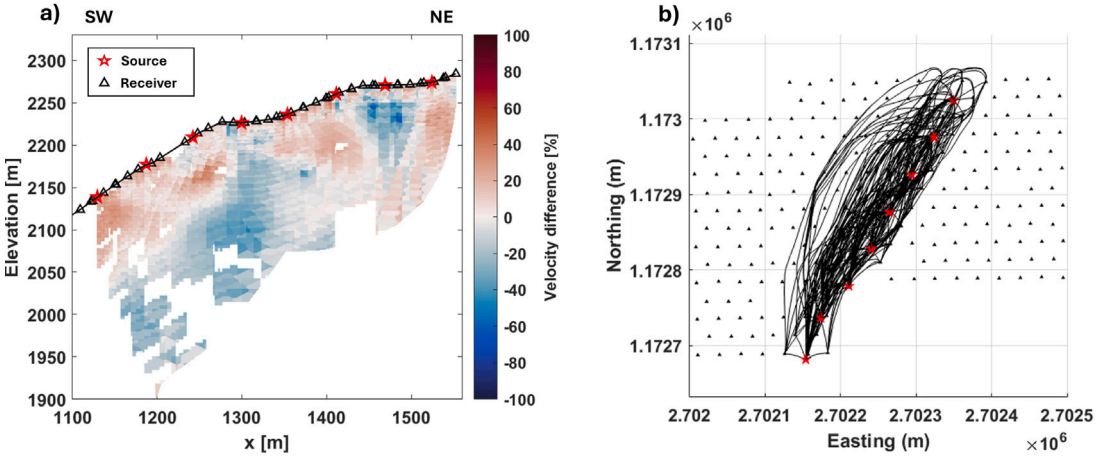

Fig. 13. (a) Relative velocity differences in percent between co-located cells in the 2D and 3D velocity model. Positive values indicate higher velocities in the 2D model relative to the 3D model, while negative values signify relative lower velocities. White cells represent regions not sampled by rays in either the 2D or 3D inversion. Source and receiver locations are marked as pentagrams and triangles, respectively. (b) Top view of the 3D shot-receiver ray paths for shot and receiver positions that were used for both the 2D and 3D inversion process. The source and receiver positions are plotted by red pentagrams and black triangles, respectively. (For interpretation of the references to colour in this figure legend, the reader is referred to the web version of this article.)

co-located plane extracted from the 3D model. Additionally, the 2D inversion incorporated three parallel receiver lines adjacent to the source line (Fig. 6), effectively approximating an elongated 3D domain within a 2D framework. This projection may introduce further inaccuracies. Moreover, the 2D and 3D models were optimized independently, each subject to domain-specific regularization constraints and corresponding inversion effects.

8.2. Model robustness and methodological limitations

The ray coverage within the upper 200 m is generally dense and adequately distributed (Figs. 8, 9 and 12) indicating that the main model features, including low-velocity zones, are well constrained by data. Moreover, a large variety of starting models and regularization constraints were tested to evaluate the stability of the inversion approach. While individual small-scale velocity details vary among resulting final models, the principal features presented in this study remain consistent throughout all inversions, irrespective of, for example, the initial model. This robustness suggests that the major velocity anomalies are data-driven rather than artifacts of regularization or local minima in the inversion process.

Nevertheless, we note that first-arrival traveltime tomography is limited by the underlying ray (high-frequency) approximation neglecting finite-frequency phenomena, such as diffraction and scattering, which limits spatial resolution. Consequently, the resulting models are relatively smooth and best suited for resolving large-scale velocity structures rather than fine-scale heterogeneities. Despite these limitations, the models presented here provide a robust representation of the subsurface, including dominant structural features that are critical for the hazard assessment of CdV. Furthermore, these models constitute

a valuable starting point for future finite-frequency or full-waveform studies that aim to refine the structural details of the unstable zone.

8.3. Vertical extent of unstable zone

At the surface, the lateral extent of the CdV unstable zone is largely constrained by surface displacement measurements (Fig. 2) obtained from total station measurements of prisms located within and outside the unstable area, a dense network of GPS measurements and digital image correlations using high-resolution orthoimages (Amann, 2006). Our 2D and 3D velocity models complement these surface observations under the assumption that low seismic velocities at depth indicate disintegrated rock. A prominent low-velocity body extends across much of the 2D profile, beginning at approximately x=500 m upslope and gradually deepening toward the CdV shoulder (Fig. 7). Just north-east of x=500 m, this damaged volume exhibits a thickness of approximately 80–100 m. Closer to the CdV shoulder, the thickness increases to 150–200 m or more, though the limited ray coverage in the 2D inversion prevents capturing the full transition to more undisturbed rock at greater depths.

The 3D model at the CdV shoulder (Figs. 9 and 10) is generally better resolved than the 2D model, extending to depths of 200–250 m in the central region. As a result, the transition from damaged to undisturbed rock is more clearly defined in the 3D model due to its deeper ray coverage. In some areas, particularly in the centre of the CdV shoulder, this transition is relatively distinct at depths of 150–200 m. However, in other regions, the transition is far more gradual and/or occurs at shallower depths. Besides that, the subsurface structure exhibits significant lateral variations at all depths. The absence of a single sharp transition at depth aligns with the proposed dynamics of Cuolm da Vi, which is considered to be of a toppling type, rather than a sharply defined failure plane.

9. Conclusions

This study presents a comprehensive 2D and 3D seismic first-arrival traveltime tomography analysis of the Cuolm da Vi (CdV) slope instability, one of the largest active mass movements in the Alps. Through an extensive field campaign deploying over 1000 seismic nodes and conducting 144 controlled-source shots, we successfully constructed high-resolution 2D and 3D velocity models, revealing significant internal heterogeneity within the unstable rock mass.

Our results highlight the presence of extensive low-velocity zones at depths exceeding 100–150 metres, suggesting substantial rock mass disintegration that cannot be detected by surface observations alone. The lateral variations in seismic velocities further emphasize the complexity of deformation processes, consistent with toppling-dominated instability mechanisms. The comparison between 2D and 3D models highlights the importance of accounting for out-of-plane effects when interpreting seismic data in highly heterogeneous alpine environments.

These findings have important implications for hazard and risk assessment. The detailed velocity models provide essential constraints for estimating the total unstable rock volume, the definition of potential hazard scenarios and can serve as input for future geotechnical and numerical stability analyses. Additionally, the results demonstrate the feasibility and effectiveness of large-scale nodal seismic deployments in alpine terrains, paving the way for further applications in monitoring and characterizing deep-seated slope instabilities.

Future work focuses on integrating seismic tomography with geological, geodetic and remote sensing observations to refine our understanding of the subsurface structure. Furthermore, additional seismic investigations, such as shear-wave tomography and localization of micro-seismicity, could provide complementary insights into the mechanical properties and structural dynamics of the CdV instability.

CRediT authorship contribution statement

Tjeerd Kiers: Writing – original draft, Visualization, Methodology, Investigation, Formal analysis, Data curation, Conceptualization. **Cédric Schmelzbach:** Writing – review & editing, Supervision, Project administration, Methodology, Funding acquisition, Formal analysis, Conceptualization. **Hansruedi Maurer:** Writing – review & editing, Supervision, Software, Methodology, Conceptualization. **Florian Amann:** Writing – review & editing, Methodology, Conceptualization. **Johan Robertsson:** Writing – review & editing, Supervision, Resources, Funding acquisition, Conceptualization.

Declaration of Generative AI and AI-assisted technologies in the writing process

During the preparation of this work the author(s) used the ChatGPT-4o model in order to perform grammar checks and provide textual suggestions for improved readability and flow. After using this tool/service, the author(s) reviewed and edited the content as needed and take(s) full responsibility for the content of the publication.

Funding sources

This research was funded by the European Union's Horizon 2020 research and innovation programme under the Marie Skłodowska-Curie grant agreement No. 955515.

Declaration of competing interest

The authors declare the following financial interests/personal relationships which may be considered as potential competing interests: Johan Robertsson reports equipment, drugs, or supplies was provided by STRYDE. If there are other authors, they declare that they have no known competing financial interests or personal relationships that could have appeared to influence the work reported in this paper.

Acknowledgements

We genuinely thank STRYDE for providing the large number of seismic nodes and for their extensive support before, during, and after the deployment. Special thanks go to Nicolas Goujon for the valuable discussions on deployment planning, node configurations, and data preprocessing. We are grateful to Disentis Bergbahnen, and in particular Marco Schmed and Simon Beer, for their continuous support and flexibility regarding the cable car rides during our field campaigns. We sincerely thank all those who supported us in the field: Aris, Christoph, Dario, David, Hagen, Janosch, Jonas I., Jonas M., Julius, Nickolas, Pascal, Patrick, Sebastian, and Timothee, for their help with the nodal deployment, retrieval, and logistics in Zurich. Lastly, we thank Christoph Baerlocher and the E-Lab for their technical assistance throughout the project and acknowledge support for this research by Landmark Graphics Corporation via the Landmark University Grant Program.

Data availability

The raw seismic shot records including first-arrival traveltimes will be made publicly available upon completion of the project (expected in 2026). In the meantime, data are available upon request.

References

Aki, K., Richards, P., 2002. Quantitative Seismology, 2nd ed University Science Books.

Alimohammadlou, Y., Najafi, A., Yalcin, A., 2013. Landslide process and impacts: A proposed classification method. Catena 104, 219–232. http://dx.doi.org/10.1016/j.catena.2012.11.013.

Amann, F., 2006. Großhangbewegung Cuolm Da Vi (Graubünden, Schweiz): Geologisch-geotechnische Befunde und numerische Untersuchungen zur Klärung des Phänomens. Universität Erlangen-Nürnberg.

Amann, F., Donatsch, G., Bonanomi, Y., Moser, M., 2006. Kinematik und Bewegungsmechanismus der tiefgründigen Instabilität Cuolm Da Vi (Graubünden, Schweiz). Bull. Angew. Geol. 11, 117–131.

Bickel, V., Manconi, A., Amann, F., 2018. Quantitative assessment of digital image correlation methods to detect and monitor surface displacements of large slope instabilities. Remote Sensing 10 (6), 865. http://dx.doi.org/10.3390/rs10060865.

Bonnard, C., Forlati, F., Scavia, C., 2004. Identification and Mitigation of Large Landslide Risks in Europe: Advances in Risk Assessment. CRC Press.

Eberhardt, E., Willenberg, H., Loew, S., Maurer, H., 2001. Active rockslides in Switzerland – understanding mechanisms and processes. In: International Conference on Landslides – Causes, Impacts and Countermeasures. pp. 25–34.

Erismann, T.H., Abele, G., 2001. Dynamics of Rockslides and Rockfalls. Springer Science & Business Media.

Froude, M.J., Petley, D.N., 2018. Global fatal landslide occurrence from 2004 to 2016. Nat. Hazards Earth Syst. Sci. 18 (8), 2161–2181. http://dx.doi.org/10.5194/nhess-18-2161-2018.

Gili, J.A., Corominas, J., Rius, J., 2000. Using global positioning system techniques in landslide monitoring. Eng. Geol. 55 (3), 167–192. http://dx.doi.org/10.1016/S0013-7952(99)00127-1.

Glueer, F., Mreyen, A.S., Cauchie, L., Havenith, H.B., Bergamo, P., Halló, M., Fäh, D., 2024. Integrating seismic methods for characterizing and monitoring landslides: A case study of the heinzenberg deep-seated gravitational slope deformation (Switzerland). Geosciences 14 (2), 28. http://dx.doi.org/10.3390/geosciences14020028.

Greenhalgh, S., King, D., 1981. Curved raypath interpretation of seismic refraction data. Geophys. Prospect. 29 (6), 853–882. http://dx.doi.org/10.1111/j.1365-2478.1981.tb01031.x.

Handwerger, A., Fielding, E., Sangha, S., Bekaert, D., 2022. Landslide sensitivity and response to precipitation changes in wet and dry climates. Geophys. Res. Lett. 49, http://dx.doi.org/10.1029/2022GL099499.

Heincke, B., Maurer, H., Green, A.G., Willenberg, H., Spillmann, T., Burlini, L., 2006. Characterizing an unstable mountain slope using shallow 2D and 3D seismic tomography. Geophysics 71 (6), B241–B256. http://dx.doi.org/10.1190/1.2338823.

Hungr, O., Leroueil, S., Picarelli, L., 2014. The Varnes classification of landslide types, an update. Landslides 11 (2), 167–194. http://dx.doi.org/10.1007/s10346-013-0436-y.

Intrieri, E., Carlà, T., Gigli, G., 2019. Forecasting the time of failure of landslides at slope-scale: A literature review. Earth-Sci. Rev. 193, 333–349. http://dx.doi.org/10.1016/j.earscirev.2019.03.019.

Jongmans, D., Garambois, S., 2007. Geophysical investigation of landslides : a review. Bull. Société Géologique Fr. 178 (2), 101–112. http://dx.doi.org/10.2113/gssgfbull.178.2.101.

Jongmans, D., Hemroulle, P., Demanet, D., Renardy, F., Vanbrabant, Y., 2000. Application of 2D electrical and seismic tomography techniques for investigating landslides. Eur. J. Environ. Eng. Geophys. 5, 75–89. http://dx.doi.org/10.3997/2214-4609.201406464.

Kannaujiya, S., Chattoraj, S.L., Jayalath, D., Champati ray, P.K., Bajaj, K., Podali, S., Bisht, M.P.S., 2019. Integration of satellite remote sensing and geophysical techniques (electrical resistivity tomography and ground penetrating radar) for landslide characterization at Kunjethi (Kalimath), Garhwal Himalaya, India. Nat. Hazards 97 (3), 1191–1208. http://dx.doi.org/10.1007/s11069-019-03695-0.

Kiers, T., Schmelzbach, C., Amann, F., Maurer, H., Edme, P., Rinaldi, A.P., Bonanomi, Y., Robertsson, J., 2026. Advancing seismic slope instability monitoring: Integrating fibre-optic and nodal array sensing. Seismica [In Press] http://dx.doi.org/10.26443/seismica.v5i1.1997.

Kleinbrod, U., Burjánek, J., Hugentobler, M., Amann, F., Fäh, D., 2017. A comparative study on seismic response of two unstable rock slopes within same tectonic setting but different activity level. Geophys. J. Int. 211 (3), 1428–1448. http://dx.doi.org/10.1093/gji/ggx376.

Lacroix, P., Handwerger, A.L., Bièvre, G., 2020. Life and death of slow-moving landslides. Nat. Rev. Earth Env. 1 (8), 404–419. http://dx.doi.org/10.1038/s43017-020-0072-8.

Lanz, E., Maurer, H., Green, A.G., 1998. Refraction tomography over a buried waste disposal site. Geophysics 63 (4), 1414–1433. http://dx.doi.org/10.1190/1.1444443.

Le Breton, M., Bontemps, N., Guillemot, A., Baillet, L., Larose, E., 2021. Landslide monitoring using seismic ambient noise correlation: challenges and applications. Earth-Sci. Rev. 216, 103518. http://dx.doi.org/10.1016/j.earscirev.2021.103518.

Li, B., Ding, L., Rajai, M., Hu, D., Zheng, S., 2018. Backtracking algorithm-based disassembly sequence planning. Procedia CIRP 69, 932–937. http://dx.doi.org/10.1016/j.procir.2017.12.007.

Malehmir, A., Bastani, M., Krawczyk, C.M., Gurk, M., Ismail, N., Polom, U., Perss, L., 2013. Geophysical assessment and geotechnical investigation of quick-clay landslides – a Swedish case study. Near Surf. Geophys. 11 (3), 341–352. http://dx.doi.org/10.3997/1873-0604.2013010.

Manning, T., Brooks, C., Ourabah, A., Popham, M., Ablyazina, D., Zhuzhel, V., Holst, E., Goujon, N., 2018. The case for a nimble node, towards a new land seismic receiver system with unlimited channels. In: SEG Technical Program Expanded Abstracts 2018. pp. 21–25. http://dx.doi.org/10.1190/segam2018-2996250.1.

Maurer, H., Holliger, K., Boerner, D.E., 1998. Stochastic regularization: Smoothness or similarity? Geophys. Res. Lett. 25 (15), 2889–2892. http://dx.doi.org/10.1029/98GL02183.

O'toole, T.B., Tranter, N., Hudson, T., Davidson, K., Dunham, C.K., Kiers, T., Schmelzbach, C., 2024. A review of some recent large-n nodal seismic experiments in Europe. In: AGU24 Conference Abstracts. pp. S52B–04.

Paige, C.C., Saunders, M.A., 1982. LSQR: An algorithm for sparse linear equations and sparse least squares. ACM Trans. Math. Software 8 (1), 43–71. http://dx.doi.org/10.1145/355984.355989.

Patton, A.I., Rathburn, S.L., Capps, D.M., 2019. Landslide response to climate change in permafrost regions. Geomorphology 340, 116–128. http://dx.doi.org/10.1016/j.geomorph.2019.04.029.

Perrone, A., Lapenna, V., Piscitelli, S., 2014. Electrical resistivity tomography technique for landslide investigation: A review. Earth-Sci. Rev. 135, 65–82. http://dx.doi.org/10.1016/j.earscirev.2014.04.002.

Podvin, P., Lecomte, I., 1991. Finite difference computation of traveltimes in very contrasted velocity models: a massively parallel approach and its associated tools. Geophys. J. Int. 105 (1), 271–284. http://dx.doi.org/10.1111/j.1365-246X.1991.tb03461.x.

Provenzano, G., Bièvre, G., Brossier, R., Garambois, S., Métivier, L., 2025. Combining interferometry and wave equation tomography for near surface characterization: 3-D imaging of the Harmalière alpine landslide. Geophys. J. Int. 243 (2), ggaf354. http://dx.doi.org/10.1093/gji/ggaf354.

Provost, F., Malet, J.P., Hibert, C., Helmstetter, A., Radiguet, M., Amitrano, D., Langet, N., Larose, E., Abancó, C., Hürlimann, M., Lebourg, T., Levy, C., Le Roy, G., Ulrich, P., Vidal, M., Vial, B., 2018. Towards a standard typology of endogenous landslide seismic sources. Earth Surf. Dynam. 6 (4), 1059–1088. http://dx.doi.org/10.5194/esurf-6-1059-2018.

Rossi, G., Nocentini, M., Lombardi, L., Vannocci, P., Tanteri, L., Dotta, G., Bicocchi, G., Scaduto, G., Salvatici, T., Tofani, V., Moretti, S., Casagli, N., 2016. Integration of multicopter drone measurements and ground-based data for landslide monitoring. In: Landslides and Engineered Slopes. Experience, Theory and Practice. CRC Press, pp. 1745–1750.

Samyn, K., Travelletti, J., Bitri, A., Grandjean, G., Malet, J.P., 2012. Characterization of a landslide geometry using 3D seismic refraction traveltime tomography: The La Valette landslide case history. J. Appl. Geophys. 86, 120–132. http://dx.doi.org/10.1016/j.jappgeo.2012.07.014.

Schmelzbach, C., Zelt, C.A., Juhlin, C., Carbonell, R., 2008. P- and SV-velocity structure of the South Portuguese Zone fold-and-thrust belt, SW iberia, from traveltime tomography. Geophys. J. Int. 175 (2), 689–712. http://dx.doi.org/10.1111/j.1365-246X.2008.03937.x.

Shen, N., Chen, L., Wang, L., Hu, H., Lu, X., Qian, C., Liu, J., Jin, S., Chen, R., 2021. Short-term landslide displacement detection based on GNSS real-time kinematic positioning. IEEE Trans. Instrum. Meas. PP, http://dx.doi.org/10.1109/TIM.2021.3055278.

Sim, K.B., Lee, M.L., Wong, S.Y., 2022. A review of landslide acceptable risk and tolerable risk. Geoenvironmental Disasters 9 (1), 3. http://dx.doi.org/10.1186/s40677-022-00205-6.

Tryggvason, A., Bergman, B., 2006. A traveltime reciprocity discrepancy in the Podvin & Lecomte time3d finite difference algorithm. Geophys. J. Int. 165 (2), 432–435. http://dx.doi.org/10.1111/j.1365-246X.2006.02925.x.

Uhlemann, S., Hagedorn, S., Dashwood, B., Maurer, H., Gunn, D., Dijkstra, T., Chambers, J., 2016. Landslide characterization using P- and S-wave seismic refraction tomography — The importance of elastic moduli. J. Appl. Geophys. 134, 64–76. http://dx.doi.org/10.1016/j.jappgeo.2016.08.014.

Whiteley, J.S., Chambers, J.E., Uhlemann, S., Wilkinson, P.B., Kendall, J.M., 2019. Geophysical monitoring of moisture-induced landslides: A review. Rev. Geophys. 57 (1), 106–145. http://dx.doi.org/10.1029/2018RG000603.

Zaki, A., Chai, H.K., Razak, H.A., Shiotani, T., 2014. Monitoring and evaluating the stability of soil slopes: A review on various available methods and feasibility of acoustic emission technique. Comptes Rendus Geosci. 346 (9–10), 223–232. http://dx.doi.org/10.1016/j.crte.2014.01.003.

Zhao, C., Lu, Z., 2018. Remote sensing of landslides—A review. Remote. Sens. 10 (2), 279. http://dx.doi.org/10.3390/rs10020279.